Supplementary Materials for: Discretizing electrodes in phase modulators for enhanced signal modulation and multi-argle spatial multiplexing

Ziyan Zhang[1], Chen Zhang[1], Zhigiang Wu[1], Zhenyu Jiang[1], Zhuochao Tie[1], Jingkun Zhuang[1], Jijin Wang[1], Songlin Zhuang[1], and Qingqing Cheng[1,2]*
[1]*School of Optical-Electrical and Computer Engineering, University of Shanghai for Science and Technology, Shanghai 200093, China and*
[2]*State Key Laboratory of Terahertz and Millimeter Waves, City University of Hong Kong, Hong Kong, China*

CONTENTS

* qqcheng@usst.edu.cn

I. DERIVATION OF THE PHASE MODULATION TERM.

According to Maxwell's equations, the wave equation can be derived as

$$\frac{\partial^2}{\partial x^2}E(x,t) - \mu_0\epsilon_0\frac{\partial^2}{\partial t^2}\left[\epsilon(x)E(x,t)\right] = 0, \tag{S1}$$

where $\epsilon(x) = \epsilon_r \ + \Delta\epsilon\,\tilde{\epsilon}(x)$ is the permittivity after modulation, which does not vary with time. Thus, Eq. (S1) can be simplified to

$$\frac{\partial^2}{\partial x^2}E(x,t) - \frac{1}{c^2}\epsilon(x)\frac{\partial^2}{\partial t^2}E(x,t) = 0, \tag{S2}$$

where $c = \frac{1}{\sqrt{\mu_0\epsilon_0}}$ is the speed of light in vacuum. Assuming a plane-wave trial solution, we write

$$E(x,t) = a(x)\,e^{-i\omega_0 t + ik_0 x}, \tag{S3}$$

Here, ω_0 and k_0 denote the carrier frequency and wavevector, respectively, and $a(x)$ is the modulation applied to the carrier wave. Substituting Eq. (S3) into Eq. (S2), we obtain

$$\frac{\partial^2}{\partial x^2}\left[a(x)e^{-i\omega_0 t + ik_0 x}\right] - \frac{1}{c^2}\epsilon(x)\frac{\partial^2}{\partial t^2}\left[a(x)e^{-i\omega_0 t + ik_0 x}\right] = 0. \tag{S4}$$

Under the slowly varying envelope approximation, $\frac{\partial^2}{\partial x^2}a(x) \ll \frac{\partial}{\partial x}a(x)$. Since $k_0^2 = \epsilon_r\frac{\omega_0^2}{c^2}$, Eq. (S4) reduces to

$$2ik_0\,\frac{1}{a(x)}\frac{\partial}{\partial x}a(x) = -\frac{\omega_0^2}{c^2}\Delta\epsilon\tilde{\epsilon}(x). \tag{S5}$$

Integrating both sides, the modulation term is solved as

$$a(x) = e^{i\gamma\tilde{\epsilon}(x)}, \tag{S6}$$

where $\gamma = \frac{\Delta\epsilon k_0 L}{2\epsilon_r}$.

II. THE IMPLEMENTATION OF AMPLITUDE MODULATION.

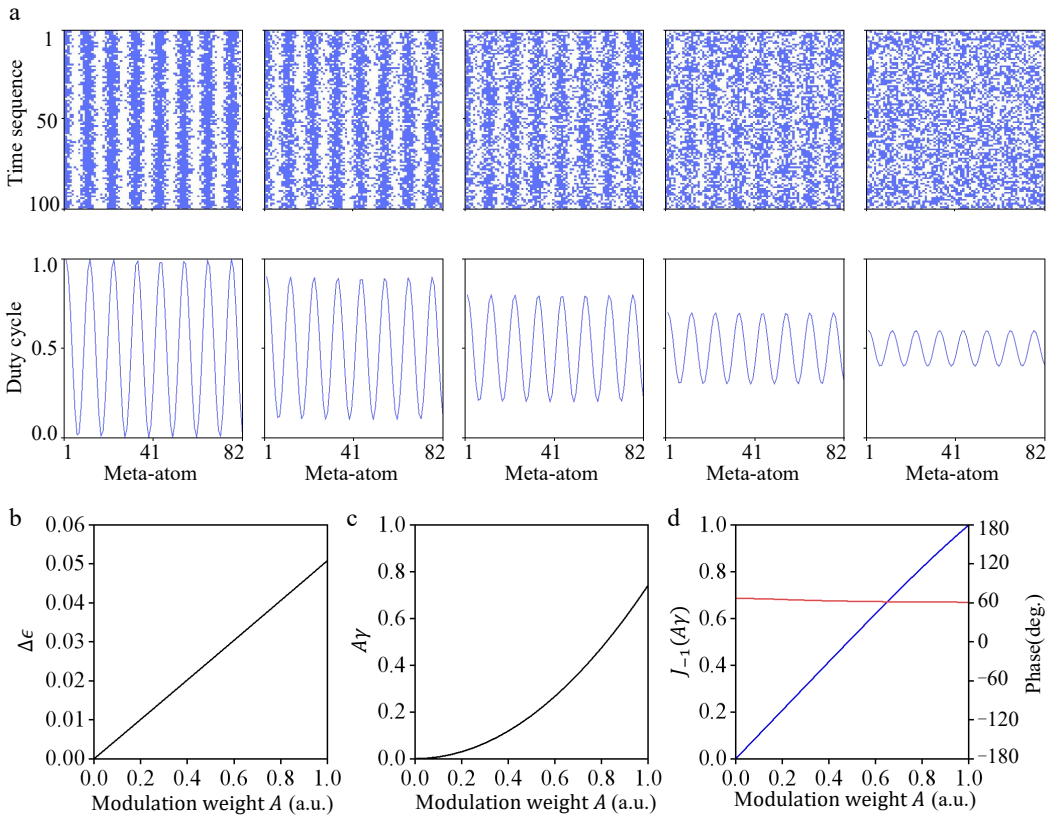

Figure S1. Approach to radiation Amplitude control.(a) The first row shows randomized STC matrices with modulation weights of 1, 0.8, 0.6, 0.4, and 0.2 respectively, while the second row displays the corresponding spatial distribution of the temporal duty cycle. (b-d) The relationship curves between modulation weight and $\Delta\epsilon$, $A\gamma$, and $J_{-1}(A\gamma)$.

Fig. S1(a) shows the randomized STC matrices corresponding to different modulation weights A. A decrease in the modulation weight A implies a reduction in the variation range of the temporal duty cycle, that is, a smaller variation in the dielectric constant, which in turn leads to a decrease in the amplitude of the radiated wave. Specifically, in the Bessel coefficient $J_{-1}(A\gamma)$, the parameter γ varies with $\Delta\epsilon$, where $\Delta\epsilon = n(A)^2 - n_0^2$. Since the value of $n(A)$ ranges only from 1.26 to 1.28, its variation is very small, and thus $\Delta\epsilon$ exhibits an approximately linear dependence on the modulation weight A, as shown in Fig. S1(b). Based on this, we obtain the curve of $A\gamma$ as a function of the modulation weight A, as depicted in Fig. S1(c). Accordingly, the theoretical amplitude $J_{-1}(A\gamma)$ versus the modulation weight A can be derived. Meanwhile, theoretical calculations indicate that the phase remains nearly unchanged with respect to A, thereby achieving effective decoupling of amplitude and phase, as illustrated in Fig. S1(d).

III. DEA DESIGN AND ITS META-ATOM STRUCTURE.

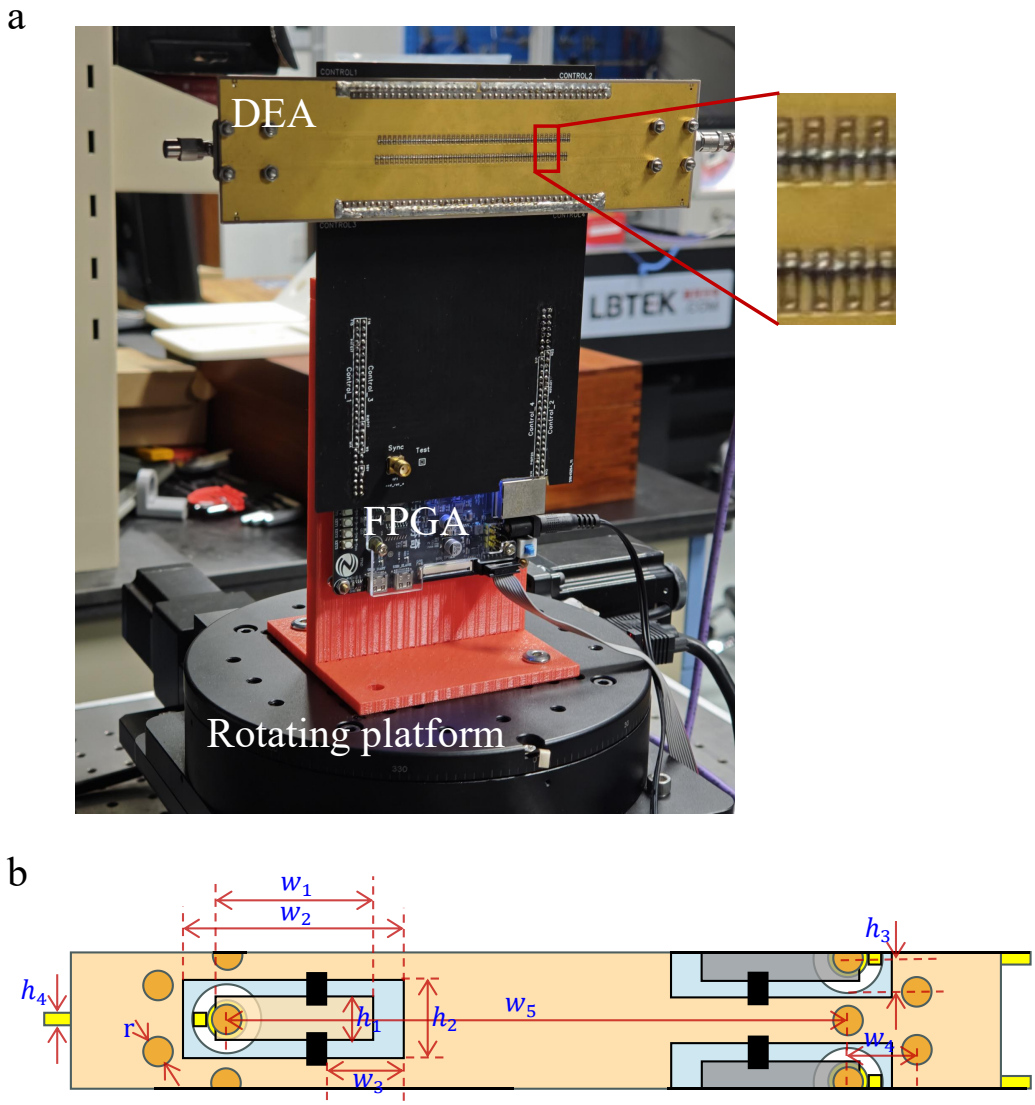

Figure S2. The detailed structure of the DEA.(a) DEA integrated with FPGA control placed on a rotating platform. (b) Metasurface unit structure on the DEA with parameters: $w_1 = 2.84\,\text{mm}$, $w_2 = 3.5\,\text{mm}$, $w_3 = 1.25\,\text{mm}$, $w_4 = 1.1\,\text{mm}$, $w_5 = 9\,\text{mm}$, $h_1 = 0.64\,\text{mm}$, $h_2 = 1.3\,\text{mm}$, $h_3 = 0.3\,\text{mm}$, $h_4 = 0.3\,\text{mm}$, $r = 2.15\,\text{mm}$.

The discrete electrode antenna (DEA) antenna adopts the architecture reported by Wu et al. (City University of Hong Kong) [1]. It consists of 82 meta-atoms on a 1 mm pitch. Each unit cell integrates two PIN diodes (MACOM MADP-000907-14020x) driven by a field-programmable gate array (FPGA) through an I/O interface. The FPGA provides 82 independently addressable bias lines, enabling per-element switching and, with timing control, space–time programmability of the DEA's effective permittivity. As shown in Fig. S2(a), a circuit board links the DEA to the FPGA; the FPGA is fixed on a rotating platform that controls the antenna's pointing direction. Figure. S2(b) shows a plan view of the meta-atom comprising plated vias, a rectangular loop slot, and two PIN diodes spanning the slot. The vias deliver isolated bias to the diodes, while the slot couples the guided field to radiation.

IV. EFFECTIVE PERMITTIVITY CONTROL VIA PWM.

PWM in essence, within one period T, the high level lasts for a duration T_{on}, while the low level lasts for $T_{\text{off}} = T - T_{\text{on}}$. The temporal duty cycle is defined as

$$\tau = \frac{T_{\text{on}}}{T}, \qquad 0 \le \tau \le 1. \tag{S7}$$

Let the FPGA output levels be V_{high} for the HIGH state and $V_{\text{low}} = 0$ for the LOW state. Then the PWM waveform within one period can be expressed as

$$v(t) = \begin{cases} V_{\text{high}}, & 0 \le t < \tau T, \\ 0, & \tau T \le t < T. \end{cases} \tag{S8}$$

Under forward bias, the effective response of a PIN diode is mainly determined by the junction capacitance. Since the junction capacitance depends on the average voltage over one period, the equivalent voltage can be defined as

$$V_{\text{eq}} = \frac{1}{T}\int_0^T v(t)\,dt = \frac{1}{T}\big(V_{\text{high}}(\tau T) + 0 \cdot (1-\tau)T\big) = \tau V_{\text{high}}, \tag{S9}$$

which shows that the temporal duty cycle τ determines the effective bias voltage applied to the PIN diode.

The junction capacitance C_d essentially arises from the storage of minority carriers near the junction under forward bias. The relationship between the stored charge and the applied voltage can be expressed as

$$Q = qA\big[n_{p0}L_n + p_{p0}L_p\big]e^{\frac{V_{\text{eq}}}{V_T}}, \tag{S10}$$

where A is the junction area, q is the electronic charge, n_{p0} and p_{p0} are equilibrium carrier concentrations, L_n and L_p are diffusion lengths, and V_T is the thermal voltage(k is the Boltzmann constant and T is the absolute temperature). On this basis, differentiating Q with respect to the voltage V_{eq} yields the diffusion capacitance:

$$C_d(V_{\text{eq}}) = \frac{dQ}{dV_{\text{eq}}} = Aq^2\frac{(n_{p0}L_n + p_{p0}L_p)}{kT}\,e^{\frac{qV_{\text{eq}}}{kT}}. \tag{S11}$$

This equation reflects that, under forward bias, the charge storage effect of minority carriers causes the charge to depend exponentially on the applied voltage, thereby determining the magnitude of the diffusion capacitance. It should be noted that this model is established under quasi-static conditions, where the operating frequency is lower than the carrier lifetime limit.

When a PIN diode is embedded in an SIW leaky-wave unit, the variation of diffusion capacitance can be equivalently regarded as a modulation of the local permittivity. The effective permittivity can be expressed as $\epsilon_{\text{eff}} = \epsilon_r + \Delta\epsilon_{\text{r}}(c)$, where $\Delta\epsilon_{\text{r}}(c)$ is related to the change in diffusion capacitance. Within the small-signal range around the bias point, the capacitance–voltage characteristic can be linearized as $\Delta\epsilon_{\text{r}}(c) \approx \alpha\big(C(V_{\text{eq}}) - C_0\big)$, where α is a structure-related coefficient and C_0 is the minimum diffusion capacitance. Therefore, by adjusting the temporal duty cycle τ, the effective capacitance of the PIN diode can be precisely controlled, thereby achieving spatial modulation of the effective permittivity within the leaky-wave unit.

V. CONSTRUCTION OF THE STC MATRIX.

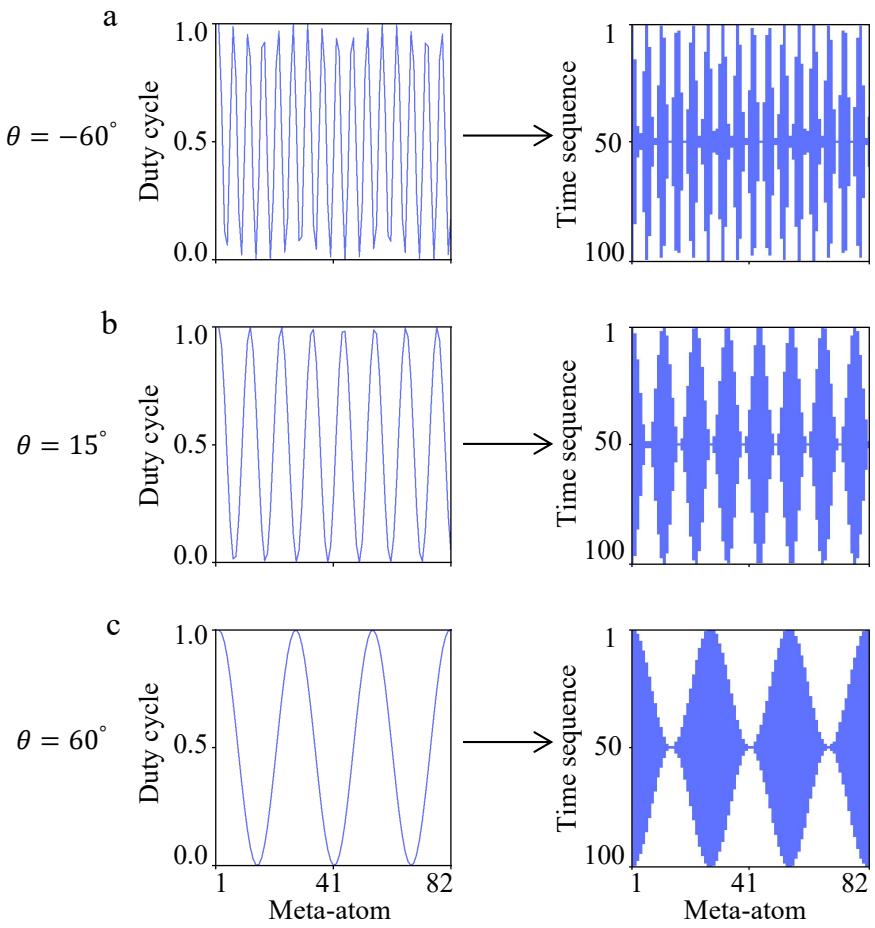

Figure S3. The conversion from time duty cycle to STC matrices.(a-c) show the distribution of temporal duty cycle and STC matrices corresponding to radiation directions of $-60°$, $15°$, and $60°$, respectively.

As an example, in Fig. S3(b), for the first PIN located at $x = 0$, Eq. (8) gives a temporal duty cycle of $\tau(x) = 1$. In the corresponding STC matrix, 100×1 modulation units are set to 1. Similarly, for the tenth PIN located at $x = 10\,\text{mm}$, the duty cycle is $\tau(x) = 0.15$, and 100×0.15 modulation units are set to 1 at this position.

VI. DERIVATION OF THE OVERLAP OF POSITIVE AND NEGATIVE ORDER FREQUENCY RADIATION MODES.

Expanding the unnormalized spatiotemporal periodic cosine modulation $\tilde{\epsilon}(x,t) = \cos(\Delta k\, x) + \cos(\Delta\omega\, t) + \cos(\Delta k\, x)\cos(\Delta\omega\, t)$ and substituting it into Eq. (2), we obtain the spectral component structure of the field as:

$$\begin{aligned} E(x,t) = & \sum_{m=-\infty}^{\infty} i^m J_m\left(\tfrac{1}{2}\gamma\right) e^{-i(\omega_0+m\Delta\omega)t+i(k_{gw}+m\Delta k)x} \\ & \times \sum_{n=-\infty}^{\infty} i^n J_n\left(\tfrac{1}{2}\gamma\right) e^{-i(\omega_0-n\Delta\omega)t+i(k_{gw}+n\Delta k)x} \\ & \times \sum_{p=-\infty}^{\infty} i^p J_p(\gamma) e^{-i\omega_0 t+i(k_{gw}+p\Delta k)x} \\ & \times \sum_{q=-\infty}^{\infty} i^q J_q(\gamma) e^{-i(\omega_0+q\Delta\omega)t+ik_{gw}x}. \end{aligned} \tag{S12}$$

By comparing the first and second terms, when $m = n$, the momentum compensation and the Bessel function coefficients are identical. This means that the radiation direction and intensity are the same. Therefore, in experiments, the radiation patterns of the $+1$ and -1 frequency orders, as well as the $+2$ and -2 frequency orders, overlap.

VII. CONSTRUCTION OF THE RANDOMIZED STC MATRIX.

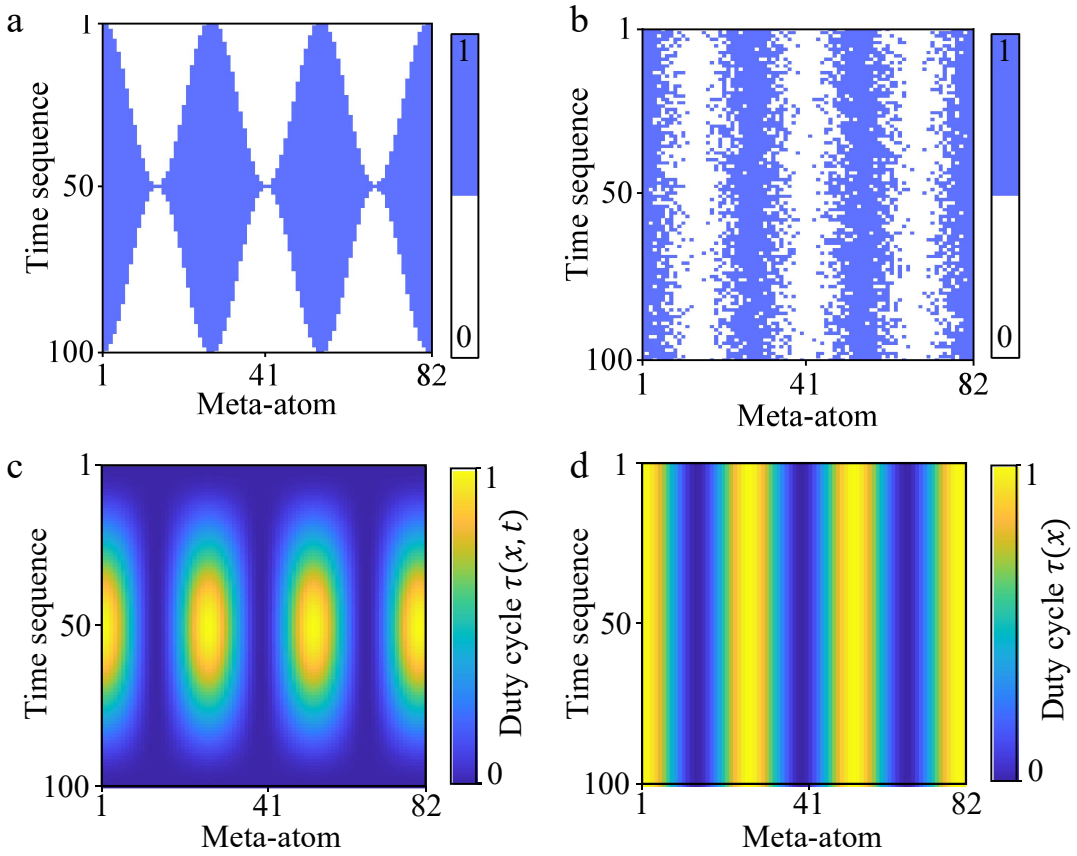

Figure S4. Comparison between unrandomized and randomized matrices.(a,c) show the unrandomized STC matrices and the corresponding temporal duty cycles at different meta-atoms and time sequences. (b,d) present the randomized STC matrices and the corresponding temporal duty cycles at different meta-atoms and time sequences.

Taking the matrix that produces a radiation direction of 60° as an example, Fig. S4(a,b) illustrates the randomization process of the STC matrix, where the "1"s in each column change from a regular arrangement to a random distribution. The corresponding duty cycles of the two matrices are shown in Fig. S4(c,d). It can be seen that after randomization, the spatial duty cycles in each temporal column are uniformly distributed without temporal periodicity, thereby suppressing the generation of higher-order spectral components.

VIII. STC MATRIX OF PHASE CONTROL AND TESTING METHOD.

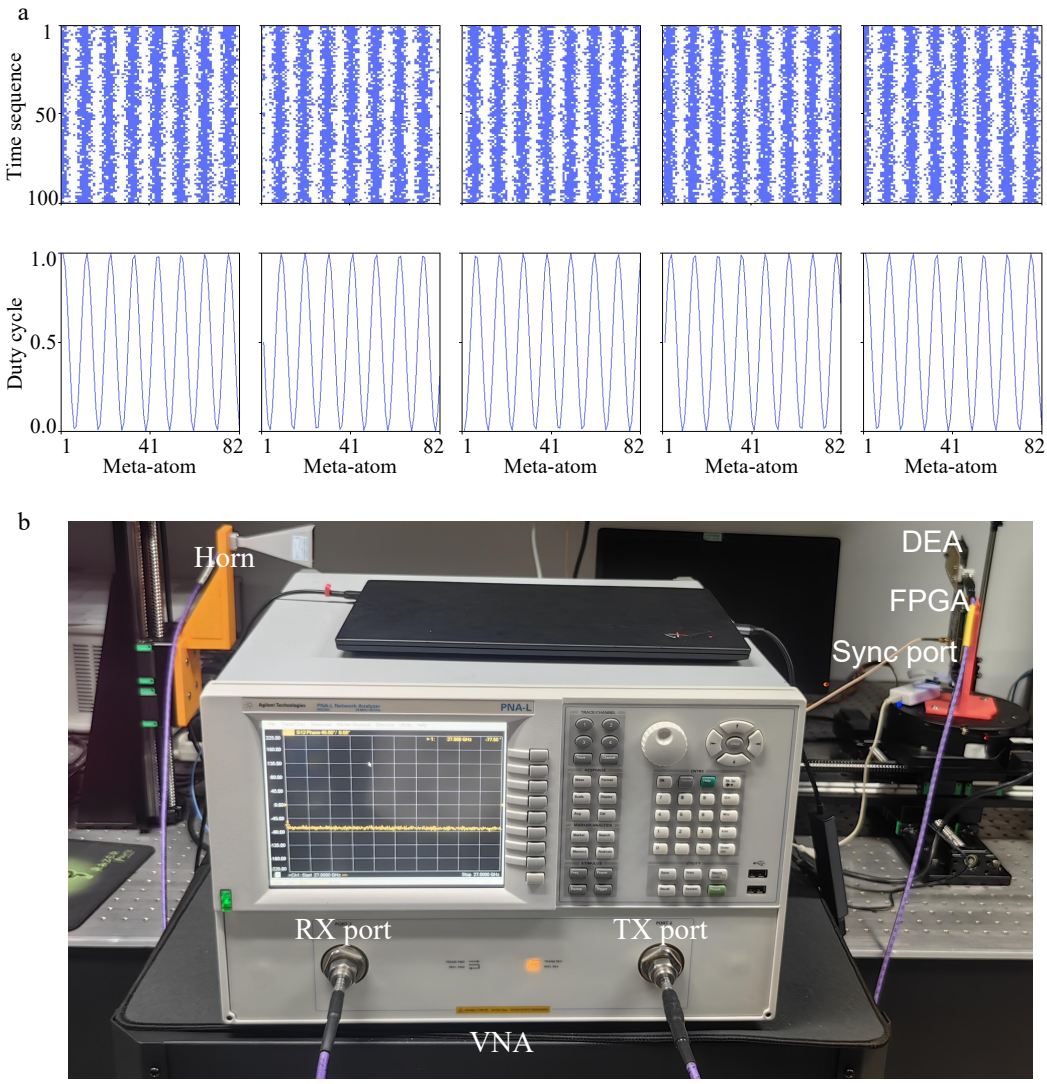

Figure S5. Approach to radiation phase control.((a) The first row shows randomized STC matrices with initial phases of 0°, 90°, 180°, 270°, and 360° respectively, while the second row displays the corresponding distribution of temporal duty cycle. (b) Phase testing experimental platform.

Fig. S5(a) shows the randomized STC matrices corresponding to different initial phase Φ.We employed a vector network analyzer (VNA) to measure the phase response of the system, Fig. S5(b). Specifically, the synchronization trigger interface of the FPGA was connected to the synchronization port of the VNA to ensure that both operated under the same clock, thereby enabling synchronous sampling. In this configuration, each time the FPGA loaded an STC matrix, the VNA synchronously acquired the corresponding signal, thus establishing a one-to-one correspondence between input and output. The transmitting port of the VNA delivered a continuous single-tone carrier signal at 27 GHz into the DEA, while the receiving port was connected to a horn antenna to capture the radiated signal from the DEA, enabling real-time measurement under the same transmit–receive frequency. During this measurement process, the phase information could be precisely extracted. The principle is that the VNA internally compares the reference channel with the measurement channel in real time, evaluating the relative phase difference between the input reference signal and the received output signal. Through vector mixing and coherent detection, the VNA provides the complex transmission parameter of the system across the full frequency range, with the phase component corresponding to the measured phase of interest.

IX. STC MATRIX LIBRARY FOR IMPLEMENTING 16QAM.

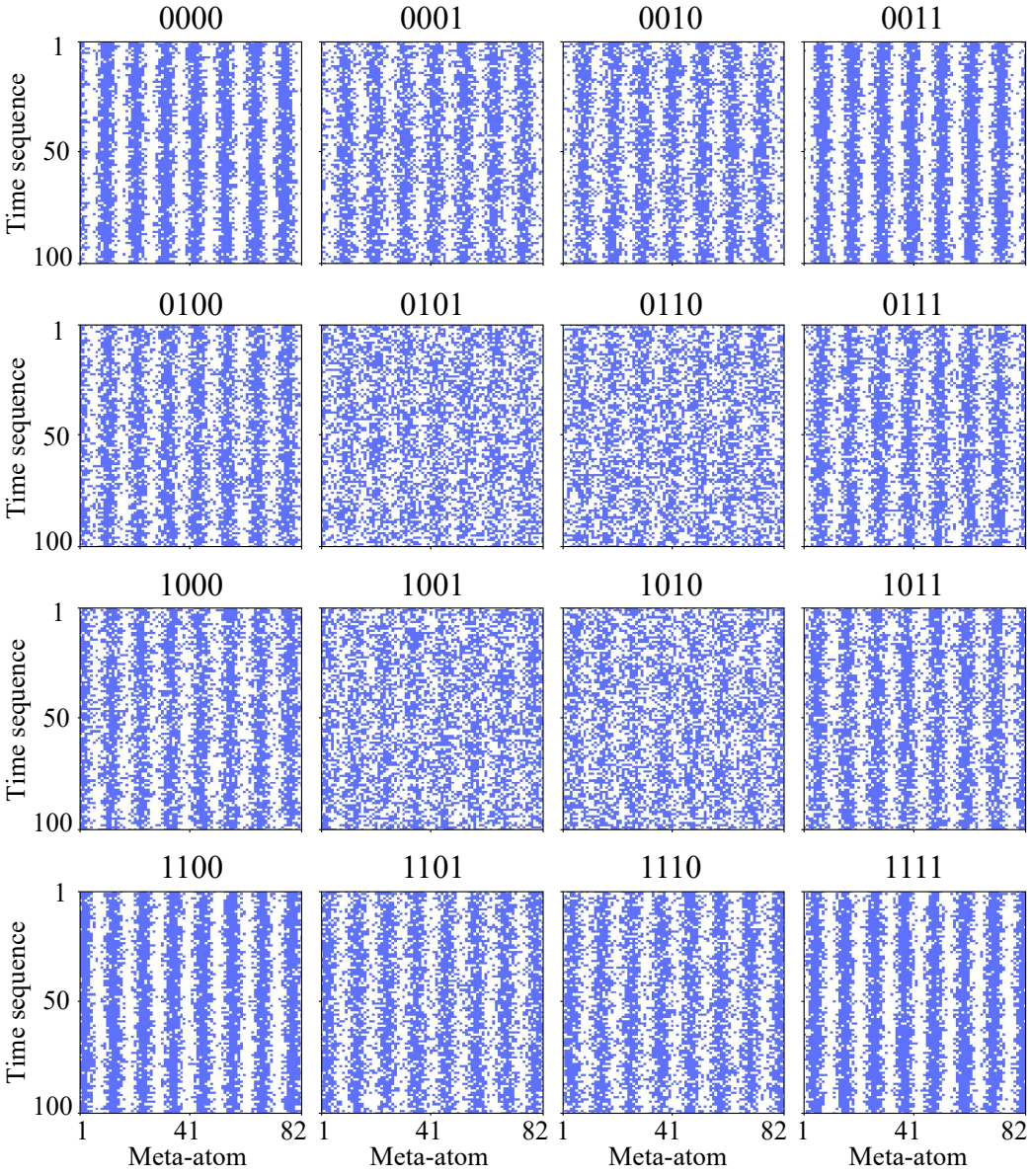

Figure S6. The mapping rules of the 16QAM constellation diagram.

Using the mapping rules of the 16QAM constellation diagram as an example to illustrate the information encoding process. The continuous binary bit stream is grouped into 4 bits per symbol, resulting in 16 discrete symbols. The mapping rule adopts two-dimensional sequential encoding and is normalized by the maximum value of the constellation points. Geometrically, the constellation diagram can be decomposed into three amplitude radii and twelve phase angles: the amplitude ratio is $1 : \frac{\sqrt{5}}{3} : \frac{1}{3}$, and the phase angles are composed of arctan(1), arctan($\frac{1}{3}$), arctan(3) and their extensions to the four quadrants.

In this work, we establish a one-to-one correspondence between symbols and STC matrices: each symbol is represented by a pre-designed STC matrix. The specific encoding order and symbol-matrix mapping are shown in Fig. S6,

and then the receiver performs demapping according to the same rule.

[1] G.-B. Wu, J. Y. Dai, Q. Cheng, T. J. Cui, and C. H. Chan, Sideband-free space–time-coding metasurface antennas, Nat. Electron. **5**, 808 (2022).